Magnetically Induced Aggregation of Iron Oxide Nanoparticles for Carrier Flotation Strategies

Schwaminger, S. P.; Schwarzenberger, K.; Gatzemeier, J.; Lei, Z.; Eckert, K.;

Originally published:

April 2021

ACS Applied Materials and Interfaces 13(2021)17, 20830-20844

DOI: https://doi.org/10.1021/acsami.1c02919

Magnetically induced aggregation of iron oxide nanoparticles for carrier flotation strategies

Sebastian P. Schwaminger,[§,†,#,*] *Karin Schwarzenberger,*[‡,⊥,#,*] *Jacqueline Gatzemeier,*[§] *Zhe Lei,*[‡,⊥] *Kerstin Eckert*[‡,⊥,*]

[§]Bioseparation Engineering Group, Department of Mechanical Engineering, Technical University of Munich, Boltzmannstraße 15, 85748 Garching, Germany

[‡]Helmholtz-Zentrum Dresden-Rossendorf, Institute of Fluid Dynamics, 01328 Dresden, Germany

[⊥]TU Dresden, Institute of Process Engineering and Environmental Technology, 01062 Dresden, Germany

[#]These authors contributed equally as co-first authors to this work

Keywords: Iron oxides, Nanoparticles, Magnetic separation, Microplastics, PMMA, Oleate, Colloidal stability, Flotation, Aggregation

ABSTRACT

On the nanoscale, iron oxides can be used for multiple applications ranging from medical treatment to biotechnology. We aimed to utilize the specific properties of these nanoparticles for new process concepts in flotation. Magnetic nanoparticles (MNP) were synthesized by alkaline co-precipitation, leading to a primary particle size of 9 nm, and coated with oleate. The nanomaterial was characterized for its superparamagnetism and its colloidal stability at different ionic strengths, with and without external magnetic field. The nanomaterial was used for model experiments on magnetic carrier flotation of microplastic particles, based on magnetically induced heteroagglomeration. We were able to demonstrate the magnetically induced aggregation of the nanoparticles which allows for new flotation strategies. Since the nanomaterial has zero remanent magnetization, the agglomeration is reversible which facilitates the process control.

Magnetic carrier flotation based on iron oxide nanoparticles can pave the way to promising new recycling processes for microplastic wastes.

1. INTRODUCTION

Magnetic iron oxide nanoparticles are among the most versatile colloids and can be used for a wide range of applications.[1,2] Their superparamagnetic behavior at room temperature and their abundance as low cost material make them attractive for multiple areas ranging from medical processing to wastewater treatment.[1,3] The nanoparticles can be synthesized via various routes and their surface properties can be tuned individually with tailored coating techniques.[1] One of the most established methods for the synthesis of superparamagnetic iron oxide nanoparticles is the co-precipitation of iron salts in alkaline environment.[4] Here, the synthesis conditions allow to control the magnetization of particles as well as their size in a range from 5 to 20 nm.[4,5] While this synthesis route is easy to reproduce, other methods such as hydrothermal and solvothermal synthesis can be employed to have an improved size distribution and shape control over iron oxide nanoparticles.[1,2,6,7]

Even though many routes, synthesis methods and protocols exist for iron oxide nanoparticles, they are difficult to store and stabilize since they tend to oxidize over time which significantly affects their magnetic and surface properties.[1] In order to solve this problem, multiple stabilization and coating strategies were developed, not only to modify the particle surface for a distinct application but to preserve the magnetic properties for long periods of processing.[8] Typically, the surface of iron oxide nanoparticles can be passivated by metal layers such as gold, which is chemically more stable than nanoscale iron oxide.[1] Another commonly used method is to introduce

a silica coating in order to keep the particles biocompatible and superparamagnetic.[1,9,10] Further approaches are based on the adsorption of carboxylic acids.[8,11,12] Here the complexation of surface iron ions by carboxyl groups can be used to establish functional groups anchored at the surface layer. Typical examples are oleate and stearate, which bind to the iron oxide surface and form a bilayer around particles.[6,13,14]

Surface modifications are not only aimed at maintaining the chemical stability but also the colloidal stability of nanoparticles in suspensions. It is a nontrivial task to stabilize iron oxide nanoparticles colloidally while still being able to separate the particles from the fluid phase in a magnetic field.[15,16] The challenge is to preserve their properties in nanoscale, e.g. the large surface area, while obtaining particles which are large enough to reduce the redistribution by Brownian motion during magnetic separation. Without magnetic field, the redistribution by Brownian motion is desired as it counteracts sedimentation and ensures a homogeneous nanoparticle dispersion over a long time. Moreover, a further coarsening of the particle size distribution after the completion of the synthesis process must be inhibited. Aggregation induced by attractive particle-particle interactions like van der Waals forces can be counteracted by repulsive forces. The electrochemical double layer which is forming at surfaces can stabilize nanoparticulate systems since identically charged surfaces repel each other. This electrostatic effect can be supported by steric stabilization with long-chain molecules adsorbed on the surface, which hinder the short distance interactions between nanoparticles by entropic effects.[17–19] In order to magnetically control and separate the particles, a further contribution is utilized, which is distinct for magnetic materials: the interaction due to magnetic dipoles.[20,21] Here, two magnetic particles orient to the respective pole and magnetically interact with each other leading to an aggregation.[12,21] With increasing aggregation diameter, the relative contribution of Stokes' drag compared with the magnetophoretic force

decreases and Brownian motion becomes negligible.[12,22] In contrast to the aggregation during storage, this magnetically induced aggregation is wanted since it significantly enhances the separation efficiency.

Indeed, not only the bottom up approach for iron oxide particle synthesis exists. Historically, iron oxides are mined and processed as ores to produce iron.[23,24] Independent of the material type, particles can reach the size of a few microns or smaller during the multiple steps of ore processing or recycling.[25] Classical separation technologies like froth flotation reach their limits for this ultra-fine particle fraction.[26,27] Carrier flotation has the potential of separating very small particles by using other particles which selectively attach at the valuable particles.[28] When magnetic particles act as carrier material, the formed particle-particle complexes can be separated from the gangue material in a magnetic field gradient.[28–31] Hence, the process can be regarded as heteroagglomeration which preferably takes place between the magnetic carrier material and the valuable particles due to their surface properties. The particle-particle complexes further grow in the magnetic field during the separation phase. By changing the composition of the continuous phase, the particle interactions are adjusted such that the carrier and valuable particles again disintegrate and can be separated in a subsequent step.[32,33] This approach overcomes a hurdle in conventional froth flotation devices, where the valuable particles are hydrophobized and attach to rising air bubbles. The mm-sized bubbles are produced by shear-induced breakup processes. Because of their low inertia, fine particles follow the streamlines of the flow around the larger bubble.[34] Besides a facilitated control of the residence time in comparison to bubbles, the size ratio between carrier and target particles can be optimized more easily, increasing the collision probability.[28] Hence, the properties of the carrier particles are essential since they determine the structure and stability of the formed aggregates.[31,35] Furthermore, the hydrodynamic conditions,

i.e. the flow field during the mixing of carrier and target particles, significantly impacts the efficiency of the separation process.[31,32,36]

Our study reveals that magnetic nanoparticles are exceptionally versatile regarding the above-mentioned features, as they are able to cover multiple size ranges by aggregation which can be tuned by hydrodynamics and the composition of the surrounding aqueous phase. Here, we investigate the interaction of oleate coated magnetic nanoparticles (MNP) with poly(methyl methacrylate) (PMMA) microspheres in the size range of 20-50 µm. The PMMA particles serve as a model system for valuable particles on the fine end of the particle size range typical for flotation. The synthetic resin as material type furthermore allows to extend our findings to the field of microplastics flotation which is regarded as a promising approach to tackle the removal of microplastics contaminations in soil and wastewater.[37,38] Therefore, we first examine how the magnetic aggregation and electrostatic stabilization can be controlled for an oleate-coated iron oxide nanoparticle system. The MNP are thoroughly characterized for their physical properties and their colloidal stability. By their modified surfaces, the nanoparticles bind to PMMA particles enabling the separation in magnetic fields. We analyze the dynamic sub-processes of attachment during the heteroagglomeration of MNP and PMMA and the magnetically induced aggregation of the formed complexes. In parallel, we determine the influence of the hydrodynamic shear on the individual steps of the magnetic carrier flotation process, i.e. the formation of MNP-PMMA complexes, the magnetic aggregation and the disintegration in the flow field. Based on these comprehensive insights, we identify potential routes to increase the performance of magnetic carrier flotation and to broaden its range of applicability as necessary steps to transfer a smart concept into a practicable technological process.

2. EXPERIMENTAL SECTION

2.1. Synthesis of MNP

A 1.8 M NaOH solution (1000 mL) was prepared with degassed deionized (dd) water and stirred (400 rpm) at 25 °C in a stirring tank reactor under nitrogen atmosphere. Iron chloride solutions, 86.4 g of $FeCl_3(H_2O)_6$ and 35 g of $FeCl_2(H_2O)_4$ were dissolved in 200 mL of dd-water each. The mixture of iron chlorides was then dosed to the sodium hydroxide drop wise. The reaction temperature was held constant for 30 minutes. The black suspension was stored under nitrogen further on and was washed several times, due to the high sodium chloride and hydroxide concentration directly after the reaction, until a conductivity below 200 µS cm^{-1} was reached.

2.2. Oleate coating

20 mL of 60 g L^{-1} sodium oleate solution were prepared with deionized water. The solution was heated to 60 °C to support solvation of the sodium oleate and stirred at 1000 rpm. 500 mL of a 5 g L^{-1} MNP-slurry was prepared with deionized water and filled into the synthesis reactor containing the oleate solution. The solution was stirred and heated at 60 °C for 1 hour. The coated particles were washed two times with deionized water.

2.3. PMMA particles

The fluorescent, polydisperse PMMA spheres with a size range between 20 and 50 µm are commercially available from microParticles GmbH (Germany) and possess a hydrophobic and slightly negatively charged surface (zeta potential around -10 mV).[39] Their size range is well detectable by optical methods such as laser diffraction and optical microscopy. The concentration of the original PMMA particle suspension was 250 g L^{-1}; PMMA density is 1.19 g cm^{-3}.

2.4. Characterization

Dynamic light scattering (DLS) measurements and zeta potential measurements were conducted with a Delsa Nano C Particle Analyzer (Beckman Coulter, Germany). Sodium hydroxide (0.1 M) and hydrochloric acid (0.1 M) were used as titrants. Particle suspensions with a concentration of 2 g L^{-1} were used for the experiments.

The particle dimensions were assessed by transmission electron microscopy (TEM) using a JEOL1400PLUS (JEOL GmbH, Germany). For the TEM measurements the colloidal samples were diluted in degassed and deionized water, ultrasonicated to disperse any agglomerates and precipitated on carbon coated copper grids (Quantifoil Micro Tools GmbH, Germany). The pictures were manually processed in ImageJ. For each sample, a minimum of four pictures was considered and at least 30 particles per picture were measured in random order.

For analysis of the solid state, the particles were lyophilized with an ALPHA 1-2LDplus (Martin Christ Gefriertrocknungsanlagen GmbH, Germany). Freeze-dried particles were analyzed gravimetrically with a simultaneous thermal analysis system (STA 449C Jupiter, Netzsch Gerätebau GmbH, Germany). The weight loss and the heat transfer of the solid samples were recorded at a heating rate of 10 K min^{-1} (323 - 823 K) under nitrogen atmosphere. The gas phase was analyzed by a mass spectrometry system (QMS 403 Aeolos, Netzsch Gerätebau GmbH, Germany). The following mass signals (amu) were recorded to identify decomposition fragments: 18 (H_2O) and 44 amu (CO_2).

Crystal structure and phase purity of the lyophilized samples were examined with powder X-ray diffraction (XRD). The measurements were performed with a Stadi-P diffractometer (STOE & Cie GmbH, Germany), equipped with a molybdenum source [Ge (111) monochromator, Mo$K\alpha_1$ radiation (λ = 0.7093 Å)] and a Mythen 1K detector (DECTRIS Ltd., Switzerland) in transmission

geometry. Data was collected in the range from 2° to 50° (2θ). The software package STOE WinXPOW (STOE & Cie GmbH, Germany) was used for indexing and refinement purposes.

The magnetic properties of the precipitates were characterized with a superconducting quantum interference device (SQUID) magnetometer MPMS (Quantum Design Inc., USA) at a temperature of 300 K. The magnetic field was varied between −50 and +50 kOe (-3979 and 3979 kA m^{-1}).

The Fourier-transform infrared spectra (FTIR) were measured using an ALPHA II (Bruker Optics, Germany) FTIR spectrometer and the matching Platinum attenuated total reflection (ATR) module. Sixty-four scans per sample and measurement were performed. Raman spectroscopy was conducted with a 488 nm laser at low laser power (0.4 mW). The baseline of IR and Raman spectra was subtracted via the concave rubber band method in the software OPUS.

For the sedimentation analysis and the magnetic sedimentation experiments a LUMiReader (LUM GmbH, Germany) with a cuvette holder containing either a permanent magnet (400 mT at surface) or a reference cuvette holder was used. Cuvettes (10x10x45 mm) were filled with 3 mL of 2 g L^{-1} nanoparticle suspension. The absorbance measurements with 870 nm, 630 nm and 410 nm lasers were conducted at 6, 10.5 and 16 mm distance to the magnet. A profile was measured every second and 200 profiles were considered for the determination of the sedimentation velocity. Magnetic flux density and gradient of the field averaged through the probe height amounted to 66 mT, and 0.14 T m^{-1}, respectively. A schematic illustration of the set-up is shown in Figure S1.

For optical centrifugation (OC), a LUMiSizer (LUM GmbH, Germany) was used. Here, the transmission at 870 nm of different centrifugation profiles from 750 to 4000 rpm were recorded and used for size distribution measurements. The density of magnetite (5.2 g cm^{-1}) was used for the analysis of transmission profiles.

2.5. Sample preparation for heteroagglomeration

Heteroagglomeration of the above-described MNP with micron-sized PMMA particles served as model system for magnetic carrier flotation. The PMMA particles were labeled with fluorescent dye (rhodamine B). This specific property allows to easily detect possible particle loss during particle size measurements (see below) and can be utilized in future work for particle tracking and determining recovery ratios. Prior to the experiments, both particle suspensions were stirred for 15 min at 80 rpm with an overhead stirrer, sonicated in an ultrasound bath for 10 min to break up weak aggregates and again continuously stirred during sampling.

2.6. Optical microscopy

Via microscopic video recordings, the small-scale dynamical processes were captured during the model carrier flotation experiments. To adjust the particle density for optical microscopy, the MNP slurry was diluted with deionized water to a concentration of 1.5 g L^{-1}. A volume of 300 µL of this diluted suspension was filled in a cuvette with 1 mm optical path length, 9.5 mm inner width and 43.5 mm inner height. Afterwards, 80 µL of PMMA suspension, diluted to a concentration of 5.5 g L^{-1}, were cautiously pipetted on top of the MNP suspension in the cuvette. The interaction of both particle systems was recorded by a CMOS camera (IDT NX4-S1 CMOS-Polaris II, 1024 pix × 1024 pix, Imaging Solutions GmbH, Germany) at a framerate of 30 Hz. The camera is connected to a long range microscope (TSO, Germany) with 50× magnification yielding a resolution of 2144.48 pix/mm. To shift the field of view, the setup is mounted on a programmable high-precision linear translation stage (LIMES 60-70-HiDS, OWIS GmbH, Germany).

2.7. Laser diffraction

Laser diffraction measurements where performed in an optical cuvette with 20 mm optical path length and 50 mm inner width and height, respectively, placed in a HELOS laser diffraction sensor (measurement range 0.9…175 µm, Sympatec GmbH, Germany). To keep the particles suspended

during measurement, a square glass blade impeller (size 12 mm × 12 mm) was inserted and agitated by a Eurostar 20 digital stirrer (IKA-Werke GmbH, Germany). It was placed 5 mm from one lateral side of the cuvette to keep the optical path for the laser beam free. The cuvette was fixed on a 27 mm wide cuvette holder with an end stop. For measurements with magnetic field, a snugly fit magnet holder was slid over the cuvette holder until it arrested at the front rim of the cuvette holder. Both holders were made from 4 mm PMMA plates. Two ring magnets (NdFeB, N 42, height 6 mm, outer diameter 40 mm, inner diameter 23 mm) were attached to the magnet holder around a circular cutout of same inner diameter to let the laser beam pass. The setup is sketched in the Supporting Information (Figure S2), together with the calculated magnetic field along the optical beam axis within the cuvette (Figure S3). Laser diffraction requires particle concentrations in a certain range for a strong and reliable signal.[40] For measurements in liquid dispersion, an optical concentration in the range of 15% to 25% is recommended, where the optical concentration is the fraction of incident light that is attenuated due to absorbance by particles. Hence, for characterizing the dynamics of MNP-PMMA-heteroagglomeration, first the PMMA system was measured as baseline at an optical concentration of 15% (corresponding to 0.125 g L^{-1} PMMA particles in 40 mL). Then, 100 µl of MNP (5 g L^{-1}) were added yielding an optical concentration of 25% and a final MNP concentration of 0.0125 g L^{-1}. The resulting particle size distributions during the formation of the MNP-PMMA complexes were taken at different time steps under continuous stirring.

Since a variety of measurement methods was employed for accessing the properties and processes of the MNP-PMMA system, Table 1 summarizes the respective methods and the obtained information for a compact overview. To validate sensitive parameters, two independent measurement approaches were used.

Table 1. Overview on employed measurement methods and resulting information.

Dynamic light scattering (DLS)	Particle size distribution of synthesized MNP
Optical centrifugation (OC)	Particle size distribution of synthesized MNP
Zeta potential measurements	Electrochemical surface properties of MNP
Transmission electron microscopy (TEM)	Primary particle size of MNP
Thermogravimetric analysis with mass spectrometry	Adsorption state of oleate on MNP surface
Powder X-ray diffraction (XRD)	Crystal structure and phase purity of MNP
Superconducting quantum interference device (SQUID)	Magnetic properties of MNP
Attenuated total reflection infrared (ATR-IR) spectroscopy	Composition of coated and uncoated MNP
Raman spectroscopy	Composition of coated and uncoated MNP
Sedimentation analysis	Sedimentation velocity of MNP with and without an applied magnetic field
Optical microscopy	Hydrodynamic processes during MNP-PMMA heteroagglomeration
Laser diffraction	Particle size distribution during MNP-PMMA heteroagglomeration

3. RESULTS AND DISCUSSION

3.1. Material and colloidal properties of synthesized iron oxide nanoparticle system

Superparamagnetic iron oxide nanoparticles were synthesized with an alkaline co-precipitation as described earlier.[4] The nanoparticles have a primary particle diameter of around 9 nm (Figures 1a, b). Similar results can be observed with TEM and Scherrer analysis of reflection broadening in XRD, which also yields a diameter of 9 nm. The signals in the diffractogram correspond to the reflections (Figure 1c): <1 1 1> at 5.4° <2 2 0> at 13.7°, <3 1 1> at 16.1°, <4 0 0> at 19.4°, <4 2 2> at 23.8°, <5 1 1> at 25.3° and <4 4 0> at 25.6°. These reflections are consistent with the standard XRD data for the cubic phase Fe_3O_4 (JCPDS no. 89-4319) with a face-centered cubic (fcc) structure.[41] The particles demonstrate a high saturation magnetization of 79 A m^2 kg^{-1} and no remanence magnetization (Figure 1d). The particles are superparamagnetic and can be approximated with a Langevin function (Figure 1d). The particles possess a high magnetization of over 40 A m^2 kg^{-1} in fields below 53 kA m^{-1}, which corresponds to the magnetic field in the magnetophoretic separation experiments.

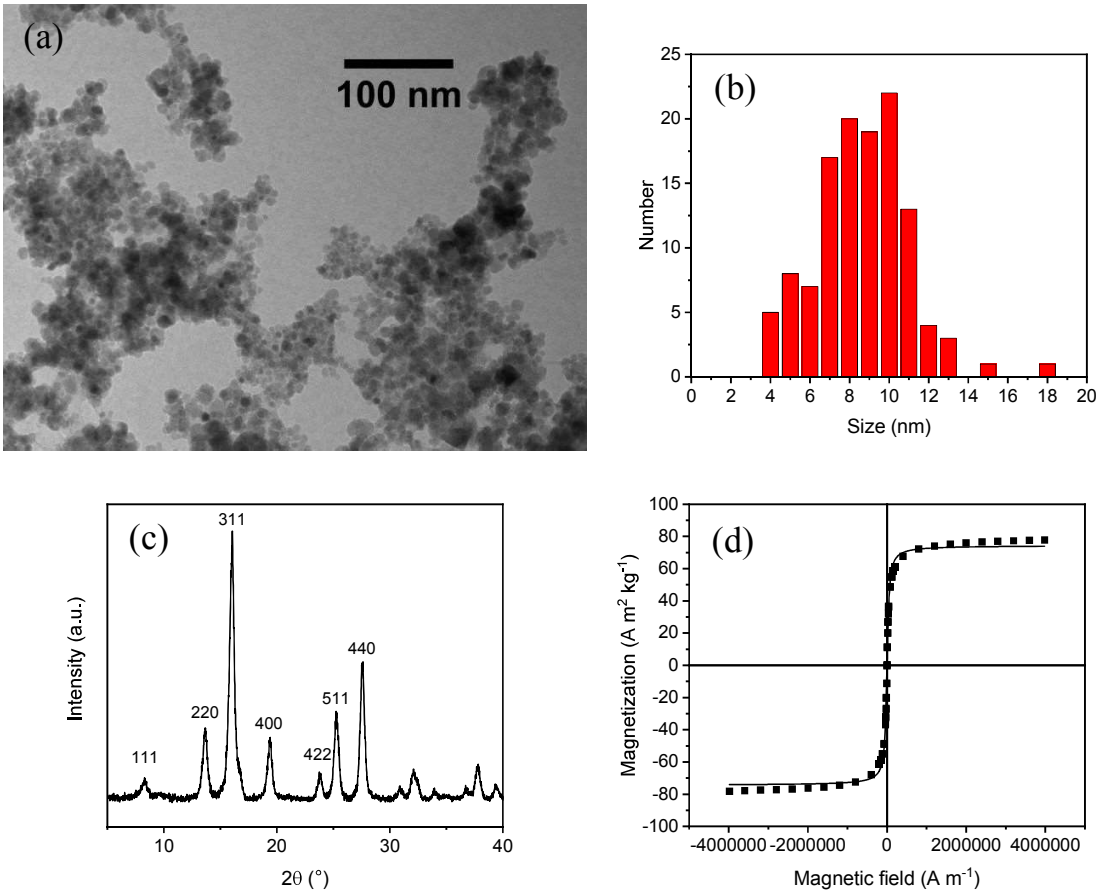

Figure 1. TEM image of synthesized iron oxide nanoparticles (a). Descriptive particle diameter statistic derived from 4 TEM images with a minimal count of 30 particles per picture (b). Powder diffractogram of nanoparticles obtained with a MoKα source (c). Hysteresis curve of the magnetization of iron oxide nanoparticles from -4000 to 4000 to 0 kA m^{-1} at 300 K obtained with a SQUID magnetometer and fitted with a Langevin function (d).

The synthesized nanoparticles mostly consist of magnetite, even though a slight oxidation can be observed with Raman spectroscopy (Figure 2a).[5,41] The bands at 666, 540 and 352 cm^{-1} refer to the Raman active modes A_{1g}, E_g and T_g, respectively. While these modes indicate magnetite as the main fraction of the synthesized nanoparticles, the shoulder at 730 cm^{-1} indicates the existence of maghemite as well. Hence, the nanoparticles used consist of a nonstoichiometric iron oxide in the transition between magnetite and maghemite.[5]

The IR spectrum also shows the presence of the T_{1u} band corresponding to spinel ordered iron oxide vibrations at 550 cm^{-1}, which confirms the presence of magnetite. Furthermore, only O-H stretch and bend vibrations can be observed at 3200 and 1600 cm^{-1}, respectively (Figure 2b). The spectrum indicates a pure and clean particle surface without any contaminations.[42]

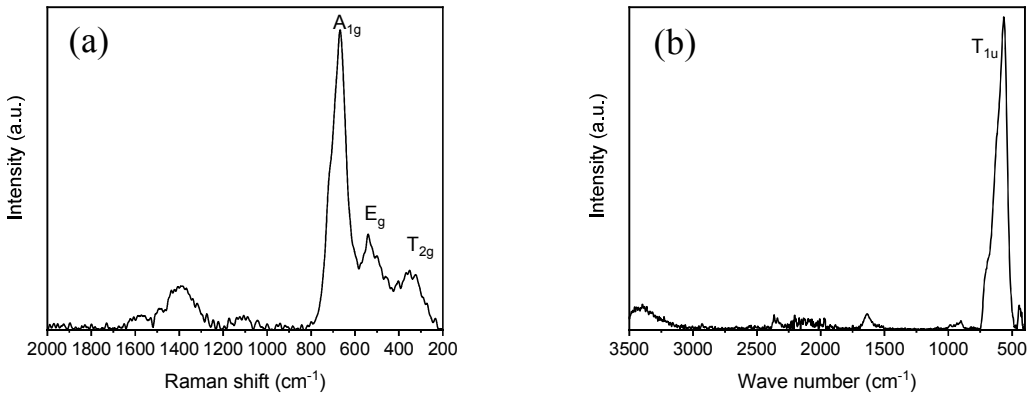

Figure 2. Raman spectrum (a) and ATR-IR spectrum of synthesized and dried iron oxide nanoparticles (b).

The synthesized nanoparticles display an amphoteric character leading to a positive surface charge at low pH and a negative surface charge at high pH. This behavior can be observed with zeta potential measurements from pH 3 to pH 10 (Figure 3a). The zeta potential of MNP ranges from 40 mV at pH 3 to -37 mV at pH 10 with an isoelectric point around pH 6.5. While a colloidal stabilization can be obtained at high and low pH values, the particles show a distinct agglomeration at neutral pH.[43] The formed agglomerates of our bare MNP at neutral pH are in the range of 300 to 600 nm (Figure 3b). This reversible agglomeration behavior can be beneficial during the magnetic separation step but

reduces the active surface area for their attachment to valuable particles.[44] Therefore, the nanoparticles need to be stabilized for an efficient magnetic carrier flotation process.

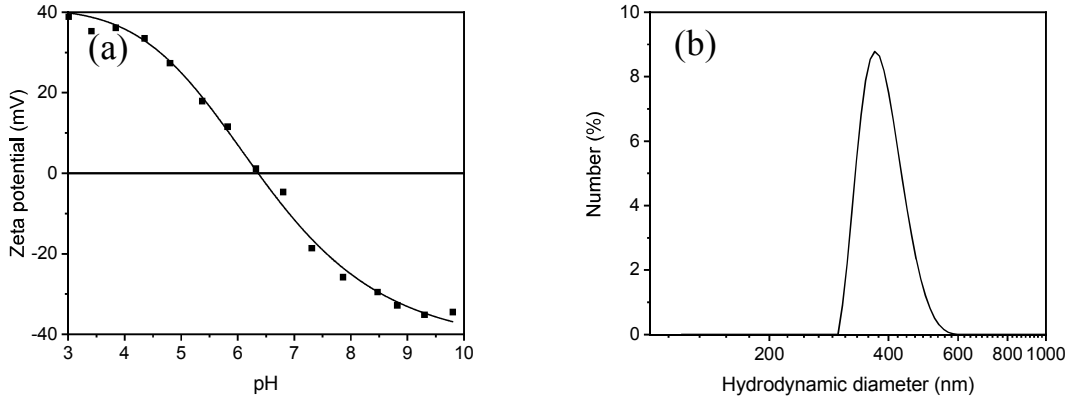

Figure 3. Zeta potential of synthesized iron oxide bare nanoparticles from pH 3 to 10 (a) and hydrodynamic diameter of the nanoparticles at pH 7 obtained with DLS (b).

A convenient way to stabilize iron oxide nanoparticles is the use of surfactants which bind to the nanoparticle surface. Here oleate is a very promising candidate, which coordinates to the surface via carboxy groups and forms a stabilizing bilayer around the nanoparticles.[13] The amount of oleate bound to iron oxide nanoparticles can be verified by simultaneous thermal analysis. For our MNP system, up to 19% of the stabilized colloid consists of oleate, which is completely degraded in two steps at 250 to 320 and at 360 to 450 °C (Figure 4, black curve). The inflection points for the second and the first layer at

280 and 395 °C, respectively, are in good agreement with literature.[7,13,14,43,45–48] The large amount of degrading material is the main indicator for the existence of a bilayer in addition to the two decomposition steps, which are also related to the formation of a bilayer.[13,14] Here a mass loss of 3% for the outer and 16% for the inner layer can be observed. CO_2 can be verified as main degeneration product which is detected by a mass spetrometer with a mass to charge (m/z) ratio of 44. Furthermore, water (m/z = 18) can be detected as other decomposition product of oleic acid as well as residual water adsorbed to the nanoparticles. The process is exothermic at both steps as can be observed from differential scanning calorimetry (DSC, blue curve). The zeta potential of the nanoparticles stabilized with an oleate bilayer is negative and indicates a stable colloid from pH 4 to 10 (Figure 4b).[8,49] The particles possess a zeta potential of -20 mV at pH 4, which decreases with increasing pH to around -45 mV at pH 7. Increasing pH further, the zeta potential becomes slightly less negative, reaching a value around -40 mV at pH 10.

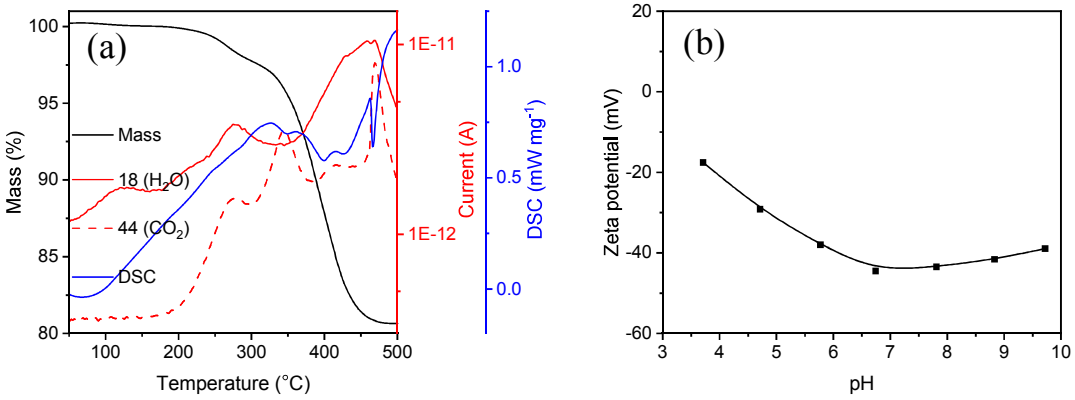

Figure 4. Simultaneous thermal analysis of freeze-dried oleate coated iron oxide nanoparticles (differential scanning calorimetry and thermogravimetry coupled with mass spectrometry) from 30 °C to 500 °C under nitrogen conditions (a). 18 H_2O (red) and 44 CO_2 (green) correspond to the red y-axis where the current is the indicator for the amount of detected m/z signals. Endothermic reactions are indicated with a positive algebraic sign in the DSC heat flow and exothermic reactions are indicated with a negative heat flow. Zeta potential of oleate coated nanoparticles from pH 4 to 10 (b).

The thermogravimetric data is supported by spectroscopic analysis of the oleate coated nanoparticles. The Raman spectrum shows a small peak at 670 cm^{-1} which corresponds to the A_{1g} mode of magnetite/maghemite (Figure 5a). Furthermore, a very prominent peak can be observed at 1600 cm^{-1} corresponding to the stretch vibration of the carboxy group

and a smaller peak can be observed at 1400 cm^{-1} corresponding to the deformation vibrations of C-H.[45,50] The ATR-IR spectroscopy investigation of the dried particles yields a similar spectrum. Here, the symmetric and asymmetric C-H stretch vibrations can be observed at 2800 and 2900 cm^{-1} (Figure 5b).[13] The stretching vibrations of the carboxy group at 1600 cm^{-1} and 1400 cm^{-1} are visible as well as the scissoring vibration of C-H at 1450 cm^{-1}.[6–8,43,45,46,50,51] In the ATR-IR spectrum, the iron oxide vibration (T_{1u}) can be observed at 550 cm^{-1}.[42]

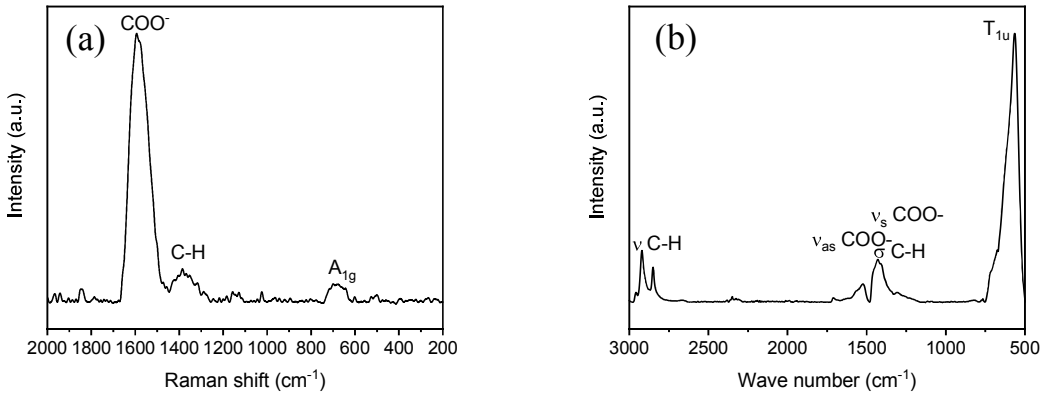

Figure 5. Raman spectroscopy of oleate coated iron oxide nanoparticles (a) and ATR-IR spectroscopy of oleate coated iron oxide nanoparticles (b).

The sterically and electrostatically stabilized oleate coated nanoparticles demonstrate a significantly lower hydrodynamic diameter of around 70 nm compared to the non-

stabilized nanoparticles with a hydrodynamic diameter of 400 nm (Figure 6b vs. Figure 3b). The diameter determined by optical centrifugation is similar to the hydrodynamic diameter determined by DLS, but slightly smaller around 50 nm together with a narrower size distribution. The discrepancy can be explained by the different size characteristic originating from Stokes' law and from dynamic light scattering.[52] Furthermore, uncertainties in using the density of magnetite (5.2 g mL^{-1}) for the oleate coated nanoparticles in the optical centrifuge add to the deviation of particle sizes obtained from both methods. The agreement of the oleate coated MNP size regarding its order of magnitude for DLS and optical centrifugation allows us to conclude that the MNP are stably dispersed in the form of small aggregates. Due to the deposition on the TEM grids, the individual aggregates cannot be distinguished on the electron microscopy images in Figure 6a. Regarding the primary particles, the shape and the appearance is similar for bare (Figure 1a) and coated MNP. Since TEM shows that the aggregates consist of primary particles in the range of a few nanometers, the synthesized MNP will provide a high specific surface area for the attachment to the PMMA particles.

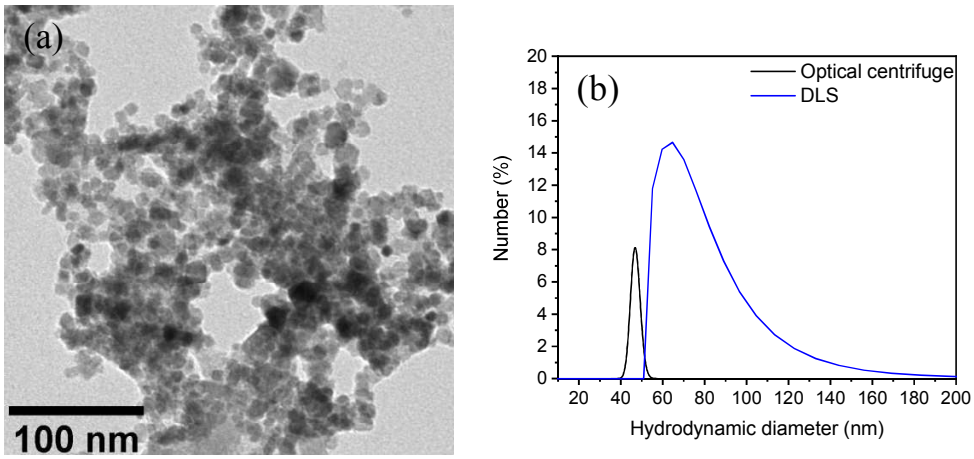

Figure 6. TEM image of oleate stabilized nanoparticles (a). Dynamic light scattering and optical centrifuge measurements of oleate coated nanoparticles (2 g L^{-1}) at pH 7 (b).

Having synthesized and characterized a nanoscale superparamagnetic particle system, which is colloidally stable, we aim to tune the particle properties in order to manipulate the system's behavior in external magnetic fields. This can be achieved by additives in the surrounding aqueous phase. A very simple way to weaken electrostatic interactions is to add salt. Therefore, we used sodium chloride for a first test of a common additive to investigate the effect on the MNP agglomerate size, and on the sedimentation with and without magnetic field. While the oleate coated particles demonstrate a very stable cumulant diameter of around 200 nm at sodium chloride concentrations ranging from 0 to 100 mM, higher salt concentrations directly lead to an aggregation of nanoparticles and

therefore to an increase of the cumulant hydrodynamic diameter of the aggregates up to 3 µm. This behavior can be observed both with DLS and sedimentation analysis (Figures 7, S4 and S5). The increase in salt concentration results in a significant increase in sedimentation velocity (Figures S6-S12). The highest sedimentation velocity is obtained at 1 M sodium chloride concentration, but even at 100 mM ionic strength, an effect on the sedimentation of nanoparticle aggregates is evident. The destabilizing effect of sodium chloride on the nanoparticle system due to the compression of the electrochemical double layer can be estimated in accordance to the DLVO (Derjaguin-Landau-Verwey-Overbeek) theory (Figure S13).[11] These calculations excellently describe the switch from stably dispersed to agglomerating MNP around 100 mM NaCl.

In a magnetic field, the salt effect is enhanced by magnetic aggregation, so that high sedimentation velocities of around 1200 µm s^{-1} can be observed at 100 mM NaCl. The DLS and optical sedimentation experiments, as well as the DLVO calculations indicate that the stability limit of the MNP dispersion is around 100 mM NaCl. As the measurement results are rather sensitive under these conditions, the additional attractive force from magnetic dipole interaction causes agglomeration and, consequently, fast sedimentation

at 100 mM NaCl. Furthermore, the gravitational sedimentation concurs with magnetophoresis which adds to the high velocities observed in the experiments with magnet. The velocity even increases with higher salt concentrations to 1750 µm s^{-1} at 5 M salt. These observations of increasing sedimentation velocity in an external magnetic field are in good agreement with literature.[53,54] Since the sedimentation velocity does not only change with the salt concentration, but also is significantly enhanced by the externally applied magnetic field (~53 kA m^{-1}), we attempt to quantify the underlying mechanisms by further calculations (SI). Such a magnetic field leads to magnetic coupling parameters λ which are larger than unity for aggregated iron oxide nanoparticles with a diameter of more than 25 nm (Figure S14).[21,55] Hence, the external magnetic field used in these experiments will induce magnetic aggregation.[53] Furthermore, the magnetic Grashof number for the particle concentration and the applied magnetic field is around 85 (SI) and indicates magnetophoresis-induced convection for the system investigated.[20,21]

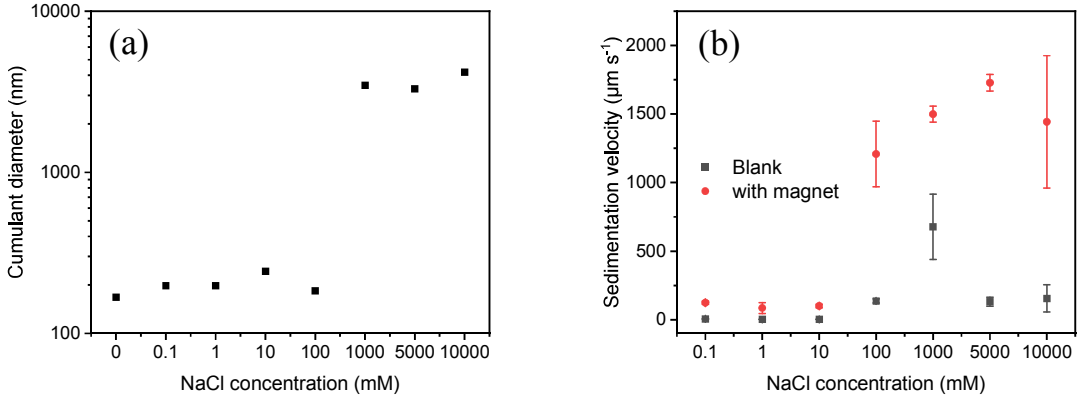

Figure 7. Cumulant diameter obtained with dynamic light scattering (a). The cumulant diameter is the Z-average diameter. Mean sedimentation velocity of oleate coated nanoparticles (2 g L^{-1}) incubated with different sodium chloride concentrations at pH 7, with and without external magnetic field (b). Standard deviations derive from experiments in triplicates.

3.2. Microprocesses during heteroagglomeration

After analyzing the surface properties of the MNP as carrier material, we now shed light on the processes occurring on the microscale during their agglomeration with PMMA particles, first without magnetic field. In carrier flotation, mixing leads to collision of carrier and microplastic particles due to their relative velocity in the flow field, and finally to

attachment if attractive interactions prevail. For optical observation, we utilize the relative velocity between the PMMA microspheres and the MNP during sedimentation in a thin cuvette (1 mm optical path). The PMMA particles were deposited on top of the MNP suspension via a pipette and the camera field of view moves from the top to the bottom of the cuvette with a speed of 150 µm s^{-1} which is approximately adjusted to their sedimentation, i.e. it corresponds to the Stokes settling velocity of a 38 µm sphere with a density of 1.19 g cm^{-3}. Large PMMA spheres settle faster than the camera movement while small PMMA spheres (and small MNP aggregates) settle slower and therefore appear in the corresponding video V1_Sedimentation.avi in the SI with an upward motion. Due to continuity, the sedimentation of the PMMA spheres additionally induces an upstream of liquid as seen at the end of V1_Sedimentation.avi when the movement of the field of view has stopped. The movement of the field of view allows to track single PMMA spheres for a longer time so that attachment events of MNP can be captured. First, we illustrate the accumulation of MNP at the PMMA surface in Figure 8. Then, we focus on exemplary attachment events in Figure 9.

The surface of the freshly added PMMA spheres in the top part of the cuvette is still mostly bare (Figure 8a, coverage ~1%). An example for a mostly bare PMMA sphere is marked by a dotted circle in Figure 8a. To provide a rough estimate for the coverage, the ratio [%] of the branched area enclosed by the outline of the attached MNP agglomerates to the projected area of the PMMA spheres is calculated for the respective images (all visible MNP-PMMA complexes manually processed in ImageJ). However, it should be noted that these values rather serve to illustrate the ongoing attachment process than to give statistically sound measurement data due to the low number of PMMA spheres in the field of view (which is needed for the optical measurement) and the stochastic collision process. With proceeding sedimentation time, the PMMA spheres are increasingly covered with MNP. Moderate coverage can be observed in the middle of the cuvette (Figure 8b, coverage ~15%), at the bottom strongly covered PMMA spheres settle into the sediment layer (Figure 8c, coverage ~120%). A moderately covered PMMA sphere is highlighted by a dashed circle in Figure 8b. The solid circle in Figure 8c labels a PMMA sphere with coverage > 100 %. This value indicates that the area enclosed by the attached nanoparticles is larger than the projected area of the PMMA sphere. The main

part of the MNP is not visible in the microscopic images (owing to the nanoscale size) and only contributes as a grey haze in the continuous phase. The presence of some agglomerates in the micron range (e.g. pointed out by the arrow in Figure 8b) allows to visualize the attachment of MNP to the PMMA spheres as described in the following.

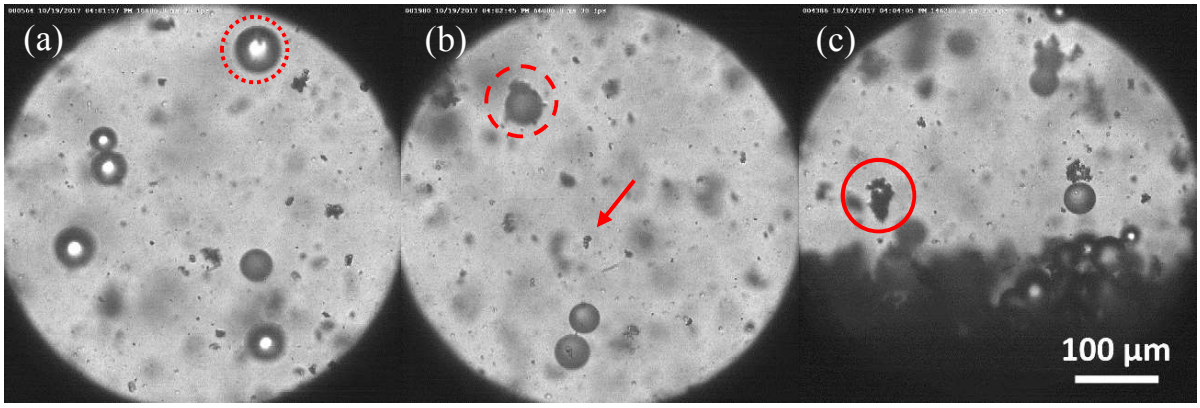

Figure 8. Increasing surface coverage during settling of PMMA microspheres through diluted MNP dispersion without magnetic field at t = 18.80 s (a), t = 66.00 s (b) and t = 146.20 s (c). Marks are referred to in the text. The process is also shown in the Supporting Information (Video V1_Sedimentation.avi).

An attachment event typically consists of three steps which are illustrated in Figure 9a-c for the interaction of an approx. 2 µm MNP aggregate (marked by an arrow) with a 42 µm PMMA sphere. Both particles first approach because of their different sedimentation

velocities as can be seen in Figures 9a, b (step 1). After the particle contact, attractive particle-particle interactions lead to the attachment of the MNP on the PMMA surface (step 2). Even though the PMMA surface is slightly negatively charged (resulting in weak electrostatic repulsion of the negatively charged MNP coated surface), attractive van der Waals forces and hydrophobic interaction between the carbon chain of the anionic surfactant and the PMMA surface prevail.[56] The formed PMMA-MNP complex then further settles in the suspension (Figure 9c). In this case, the attached MNP aggregate does not influence the sedimentation notably because of its small size compared to the PMMA sphere.

A different size ratio of PMMA sphere to MNP aggregate is depicted in the lower row, Figure 9d-h, which shows a cluster of 16 µm MNP and 28 µm PMMA. If both particles are in a similar size range, the freshly formed PMMA-MNP cluster reorients in the flow field. This reorientation affects the attachment of further MNP afterwards, since the bare side of the PMMA sphere again is facing the incident flow.

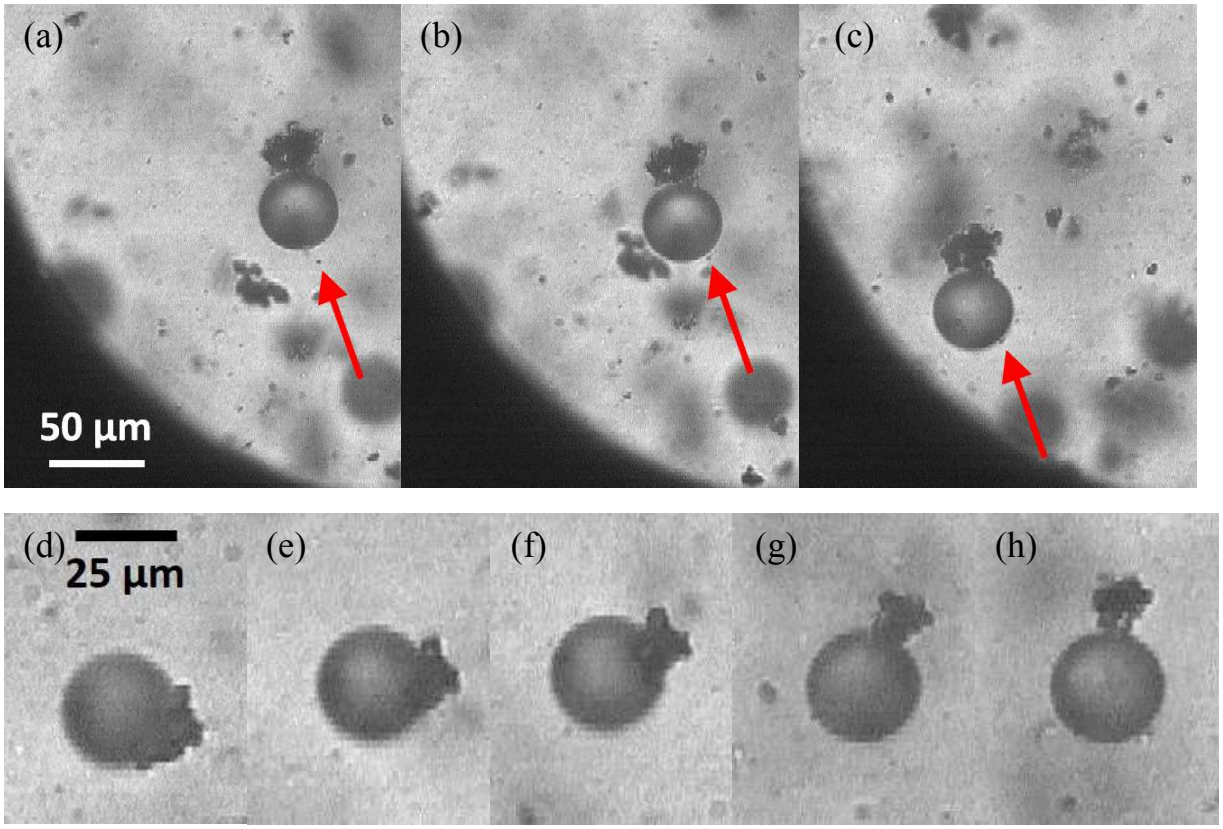

Figure 9. Attachment of a 2 µm small MNP aggregate (a-c, indicated by the arrow) to a 42 µm PMMA sphere. Pictures obtained after t = 131.50 s (a), t = 131.73 s (b) and t = 133.33 s (c). Reorientation of a freshly formed MNP-PMMA (16 µm/28 µm) cluster in the flow field during sedimentation (d-h). Pictures are taken after t = 135.00 s (d), t = 135.50 s (e), t = 135.83 (f), t = 136.67 s (g) and t = 138.33 s (h).

3.3. Aggregation and separation in a magnetic field

During magnetic carrier flotation, large clusters of carrier and microplastic particles are formed by magnetic induced aggregation which can be directed to the desired location in the container and separated.[29,31] After the magnetic field is removed, the large clusters disaggregate again so that most of the carrier particles can be recovered. Figure 10 visualizes these dynamic processes for the MNP-PMMA system by superposing the microscope images with the calculated velocity vector field from the particle movement. In Figure 10a, the PMMA microspheres already are well covered with MNP by premixing both systems before the experiment. The particles settle in the gravitational field (velocity vectors at MNP-PMMA complexes point downwards, parallel to the direction of gravity) and the camera view stays fixed. The velocity vectors are determined by dividing the image in finite interrogation windows and computing the spatial shift of grey values between two consecutive images via cross-correlation (software DaVis, LaVision GmbH, Germany).

When a small magnet (NdFeB N 42, diameter 4 mm, height 6 mm) is approached to the outer wall of the cuvette 5 mm above the field of view, the downwards velocity of the particles is reversed and they move into the direction of the magnet, i.e. the velocity

vectors point upwards in Figure 10b. However, the movement differs between the individual MNP-PMMA complexes. Their upwards drift depends on the size of the PMMA sphere, the coverage with MNP, and the interaction with the glass wall of the cuvette. Small PMMA spheres (~28 µm) with a large amount of attached MNP are strongly attracted by the magnet (long red arrows) while large PMMA spheres with a relatively low amount of MNP only move slowly in the upwards direction (short blue arrows). Large clusters of MNP and PMMA microspheres are formed in the magnetic field. Frequently, branches of MNP aggregates connect several PMMA microspheres (e.g. bottom center in Figure 10b). When the magnet is taken off in Figure 10c, the particles again switch to sedimentation (velocity vectors point downwards again). Simultaneously, the huge amount of MNP which accumulated by magnet-induced aggregation detaches and is redispersed by the flow. An example for a PMMA sphere covered by MNP is marked by a circle in Figure 10b which disintegrates in Figure 10c to a weakly covered PMMA sphere (upper circle) and fragments of the formerly large MNP aggregates (lower circle). The reorientation of formed MNP-PMMA clusters in the flow field occurs within a few seconds.

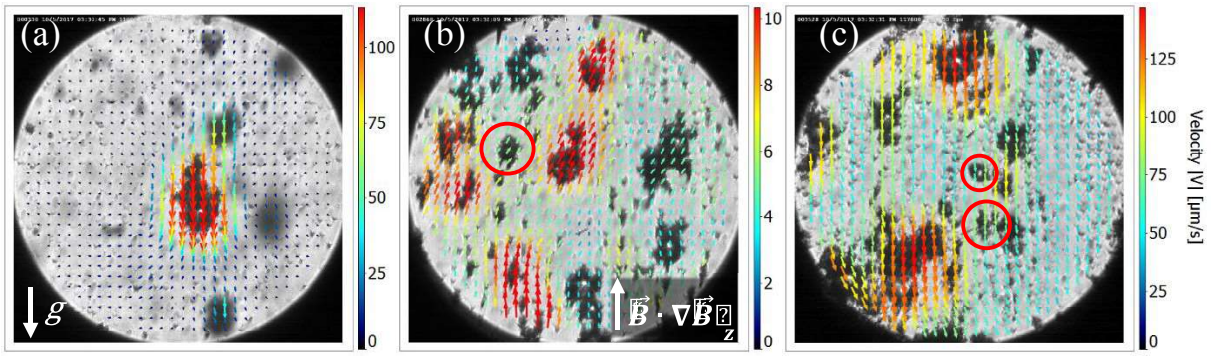

Figure 10. Particle movement during magnetic carrier flotation model experiments. (a) Sedimentation of PMMA spheres covered with MNP. The white arrow points out the direction of gravity. (b) Reversal of sedimentation velocity by applying a magnet in the top part of the cuvette. The white arrow points out the magnetic field gradient in vertical (z) direction (c) Removal of magnet: the formed larger agglomerates disaggregate; marked by circles in (b,c) for an exemplary MNP-PMMA agglomerate. The process is also shown in the Supporting Information (Video V2_Reversal.avi).

The process illustrated in Figure 10 is quantified in Figure 11 by the averaged vertical velocity component v_z of the calculated vector field. In the beginning, the vertical velocity is negative due to the sedimentation of the initial MNP-PMMA complexes. After the magnet is applied at approx. 5 s, the vertical velocity crosses zero and takes slightly positive values caused by the movement of the aggregates towards the magnet. Much

stronger flow reversal is observed if a larger magnet is used (see Supporting Information, Video V3_Magnet_dia1.avi for a NdFeB N 42 magnet with diameter 10 mm, height 10 mm). However, the extremely bulky MNP-PMMA clusters appearing in that case obstruct the optical observation by covering the whole field of view. If the aim of the process is only to separate the solid from the liquid phase, the magnet should rather be placed on the bottom of the cuvette so that sedimentation and magnetophoresis act in the same direction and the solid collects quickly at the bottom. However, to separate one particle type from others, magnetophoresis of the MNP-particle complexes should be directed antiparallel to gravity (as shown in Figure 10 and 11) so that other particle materials without attached MNP settle down.

Removing the magnet at around 105 s leads to very high negative velocities, because the MNP-PMMA clusters before significantly increased in size and effective density due to the magnet-induced aggregation of MNP. The strong variation of the averaged vertical velocity is caused by clusters of different sizes crossing the field of view. A huge mm-sized cluster generates the negative peak at 124 s. With proceeding disintegration of the

clusters, the sedimentation again slows down, i.e. the averaged vertical velocity becomes less negative.

In general, the velocity curve comprises the velocity vectors of the entire field of view in Figure 10. Hence, also remaining weakly covered PMMA spheres, which still sediment under an applied magnet, contribute to the average vertical velocity. Possible backflow of the surrounding liquid around the moving PMMA spheres due to continuity also contributes to the average vertical velocity. However, the general sequence depicted in Figure 11, i.e. sedimentation – reversal of movement – sedimentation is reproduced as can be seen from comparing with video V2_Reversal.avi in the SI.

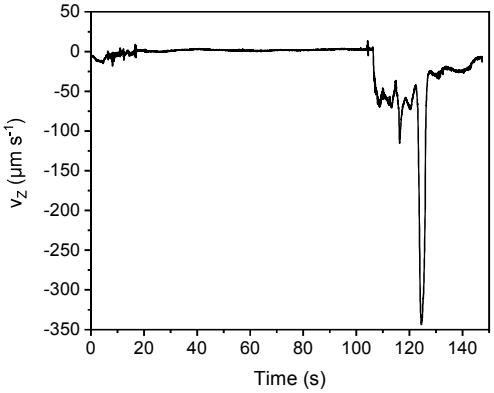

Figure 11. Average vertical velocity component of the vector field (Figure 10) during the movement of MNP-PMMA complexes under the influence of gravitational and external magnetic field (applied permanent magnet from 5 to 105 s) over time.

3.4. Evolution of particle size distribution during heteroagglomeration

The optical microscopy measurements provide detailed insights of exemplary sub-processes during magnetic carrier flotation. Additionally, measuring the particle size distribution by laser diffraction gives information on the properties of the whole ensemble. In line with the microscopy measurements, we first characterize the formation of MNP-PMMA complexes without the influence of an external magnetic field. In contrast to the thin microscope cuvettes where the particle movement resulted from sedimentation, the system now is stirred at a defined speed to approach the situation in a technological process.

The volume-weighted particle size distribution was measured at different times up to t = 18 min for a stirring speed of 600 rpm within the laser diffraction cuvette. The particle size distribution curves are shown in the Supporting Information (Figure S15). Here, we

summarize the main trends in the size distribution curves without magnetic field by using $x_{90,3}$. The value $x_{90,3}$ is the particle size at which 90% of the particle volume in the measurement range is smaller, and thus characterizes the coarse part of the size distribution. The increasing coverage of the PMMA spheres with MNP in the mixing flow of the stirrer appears as a slight shift to larger particle sizes with time, as $x_{90,3}$ = 50.3 µm at t = 0 min and $x_{90,3}$ = 65.7 µm at t = 18 min. To exclude that the effect is caused by the sole aggregation of PMMA particles, the experiment is repeated without MNP. No clear increase in particle size is observed in that case ($x_{90,3}$ = 49.1 µm at t = 0 min and $x_{90,3}$ = 49.6 µm at t = 18 min, also see Figure S16). This shows that the above-described observation is indeed the characteristics of the MNP-PMMA heteroagglomeration. The continuously coarsening size distribution suggests that abrasion of attached nanoparticles by collision of their host micron-sized particles as observed by Dong et al.[57] is not dominant for this MNP-PMMA system.

To analyze the magnet-induced agglomeration of MNP with PMMA microspheres, the time-dependent particle size distribution was monitored for the setup with inserted magnet holder at different stirring speeds. The minimum stirring speed (500 rpm) is set such that

particle sedimentation is counteracted. The maximum stirring speed (800 rpm) is determined by the formation of air bubbles within the vortex at the stirrer blade.

During the mixing process with applied magnet, the particles agglomerate but at the same time migrate in the magnetic field gradient towards the walls of the cuvette and accumulate at the glass near the ring magnets. Hence, only a slight increase in particle size can be observed in Figure 12a from 0 to 18 min (for 600 rpm $x_{90,3}$ = 49.8 µm at t = 0 min and $x_{90,3}$ = 59.2 µm at t = 18 min). After 18 min, the magnet holder is removed. The resulting release of large MNP-PMMA clusters leads to a pronounced shift to larger particle sizes at 19 min (for 600 rpm $x_{90,3}$ = 123.6 µm). This is visible by the lower values of the cumulative function Q_3 for large x. In the density function q_3 at t = 19 min, the peak around 40 µm decreases and higher values are reached for large particle sizes (x > 60 µm). Subsequently, the formed large aggregates are partly redispersed and the coarse particle fraction is reduced again from 21 to 33 min (for 600 rpm $x_{90,3}$ = 102.0 µm at t = 21 min and $x_{90,3}$ = 95.9 µm at t = 33 min).

The process of agglomeration and redispersion strongly depends on the stirring speed. With increasing stirring speed from 600 rpm (Figure 12a) to 800 rpm (Figure 12b), a larger

shear force acts on the weakly bound agglomerates so that only smaller agglomerates are formed and they are dispersed again more efficiently. Therefore, at 800 rpm and t = 19 min, Q_3 is not much reduced for large x, and the distribution curves before and after the removal of the magnet differ only slightly. The stirring intensity likewise can be adapted to the different process steps. Our results on the dependence of the aggregate size on the stirring speed suggest that larger MNP-PMMA clusters form by magnet-induced aggregation under moderate stirring, while the redispersion of the carrier material is more effective under intense stirring.

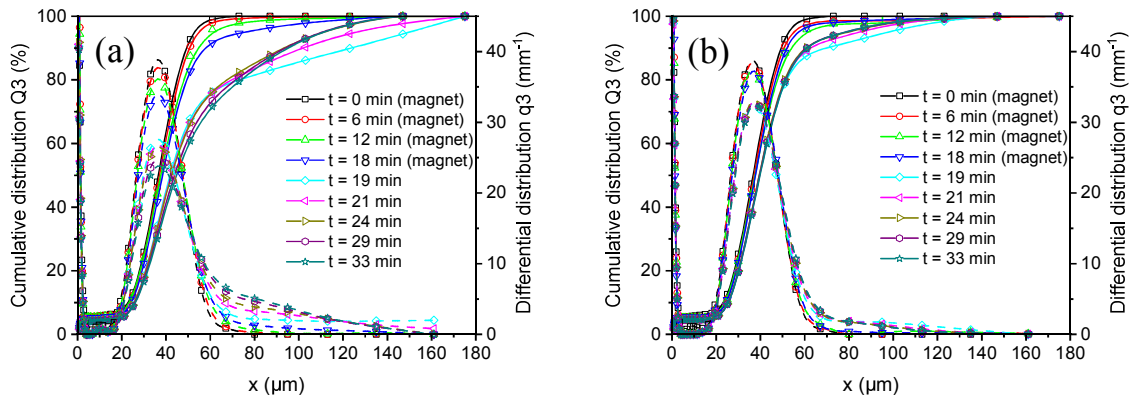

Figure 12. Particle size distributions (volume-weighted cumulative function Q_3 and density function q_3) of the PMMA + MNP suspension when applying a magnetic field and removing the magnets again. Cumulative distribution is illustrated by full and differential

distributions by hatched lines. The suspensions are stirred at different stirring speeds: (a) 600 rpm and (b) 800 rpm.

Figure 13 illustrates the coarse particle size $x_{90,3}$ as a function of the stirring speed. Three curves are included in this graph for three characteristic times: first, at the end of the magnetization at t = 18 min (black curve “Magnet on”); second, immediately after the removal of the magnet holder at t = 19 min (red curve “Magnet off”); and third, at t = 33 min (blue curve “Redispersion”), when a large part of the formed aggregates has been redispersed. Each measurement point is determined as an average value from three independent heteroagglomeration experiments, along with the standard deviations as error bars.

The approximately constant values for $x_{90,3}$ at the end of the magnetization (black curve) probably are caused by the migration of the MNP-covered PMMA particles out of the measurement beam towards the ring magnets. The aggregation mainly takes place in the regions near the cuvette wall where the magnetic field gradients are high (Figure S3). Thus, the stirring speed has no huge influence on $x_{90,3}$ at this stage. With removal of the

magnet (red curve), the formed large aggregates are released into the fluid volume and hence can be detected in the measurement beam. This leads to a jump to high $x_{90,3}$ values from the black to the red curve. The large aggregates then disintegrate with time in the shear flow of the stirrer (blue curve). Both the curve after the removal of the magnet and at the end of the measurement show a distinct decrease at higher stirring speed on account of the higher shear in the flow field. The plateau in the beginning (< 600 rpm) indicates a balance between the effects of enhanced collision and enhanced redispersion with more intense stirring. For stirring rates > 600 rpm, the redispersion effect dominates. At the highest stirring rates, the difference between the curves before and after the removal of the magnet vanishes. This suggests that the accumulation of aggregates at the walls of the cuvette is almost completely suppressed at 800 rpm.

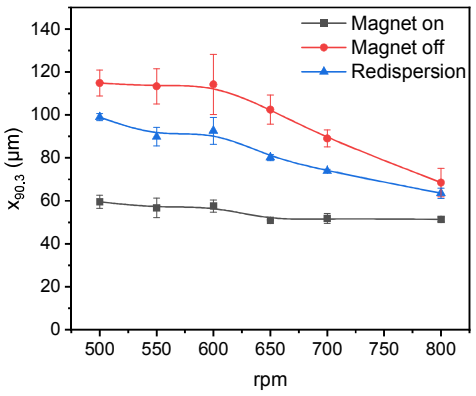

Figure 13. Dependence of MNP-PMMA aggregate size on stirring speed at characteristic stages of magnetically induced aggregation and redispersion by the shear forces.

4. Discussion

The measurements presented in the previous sections successfully reproduce central aspects of magnetic carrier flotation. Nevertheless, the experimental constraints introduce certain limitations which we discuss in the following. Thereafter, we transfer our findings to the technological process.

An important restriction is that the experimental conditions had to be adapted to the individual measurement methods. The first difference concerns the employed particle concentration and ratio of MNP to PMMA. To provide the best optical observability, a higher particle concentration was used in the thin optical cuvette for microscopy compared to the particle concentration in the thick stirred cuvette for the laser diffraction measurements. Hence, a noticeable coverage of PMMA spheres with MNP is achieved in the microscopy experiments even in the shorter duration and weaker mixing of the particle sedimentation from the top to the bottom of the cuvette. Furthermore, different

permanent magnet types and positions were chosen as dictated by the specific device setups. For the sedimentation analysis in the LUMiReader, the magnet had to be fitted in the cuvette holder. For the laser diffraction measurements two ring magnets were chosen which were suitable for the larger cuvette size and assured an axisymmetric configuration with respect to the laser beam axis. An exact and reproducible positioning of the magnet for the 500 µm sized field of view in the microscopy measurement was difficult especially in the horizontal direction. Hence, the microscopic observations of magnet-induced agglomeration rather serve as proof-of-concept due to these uncertainties. Nevertheless, particularly the combination of different methods allowed for comprehensive insights into the underlying physics which can serve as a knowledge base for future technological applications as specified hereafter.

4.1. Optimization of process conditions

The reorientation of formed MNP-PMMA clusters in the flow field occurs within a few seconds. This can be used to estimate if reorientation is effective in a large-scale reactor depending on the time scale and the structures of the flow field, what impacts the further attachment of MNP carrier material. Laboratory experiments on the migration velocity of

the MNP-PMMA clusters depending on the MNP coverage might be applied to optimize the required MNP ratio and the conditioning time, i.e. the duration of premixing the MNP carrier material with the particles to be separated. This is especially important in order to control the magnet-induced aggregation as well as the magnetophoresis-induced convection which are strongly dependent on the particle concentration.[21]

4.2. Aggregate structure

The branched shape of the MNP-PMMA clusters which grow during magnet-induced aggregation is advantageous in several respects of the technological process. First, through controlled aggregation of the MNP, different scales from nano to micro can be covered allowing to adjust the carrier size to the size of the target particle system. Second, the aggregate structure provides a bridging effect between different MNP-PMMA clusters, so that remaining weakly covered PMMA are integrated in larger clusters and subsequently undergo magnetic separation. Third, the small primary particle size of the MNP involves a high surface-to-volume ratio, i.e. a large available area to attach to the PMMA particles. In our experiments, a few coarse agglomerates were present which were used to visualize the MNP-PMMA attachment via optical microscopy. The investigation

of the colloidal properties of the MNP however showed that the main part of the carrier material is stably dispersed and only is subject to heteroagglomeration with the PMMA microspheres and magnet-induced aggregation.

4.3. Additives

The potential to modify the surface properties of the MNP system, and hence the particle-particle interactions, is demonstrated by the measurements with salt addition. For the removal of contaminants from sea water, the studied salt-related effects naturally have to be considered. In view of general carrier flotation processes, a pre-agglomeration step with such an easily available and cheap additive offers a further means to control the carrier particle size and to facilitate the magnetic separation of the bound particles. After the separation, a flushing step with low ionic strength solution can be employed to support redispersion of the carrier material.

4.4. Hydrodynamic shear

The stirring intensity likewise can be adapted to the different process steps. Our results on the dependence of the aggregate size on the stirring speed suggest that larger MNP-

PMMA clusters form by magnet-induced aggregation under moderate stirring, while the redispersion of the carrier material is more effective under intense stirring.

4.5. Selectivity

Strictly speaking, our current experiments on the MNP-PMMA material system rather fall into the category of magnetic separation than magnetic carrier flotation. For the latter, the carrier material selectively binds to target grains in a mixture of particle materials.[58] However, our findings are likewise applicable here since they treat a subset of this larger problem. For example, considering the removal of microplastic material from sand, the oleate coated magnetic carrier material can be expected to attach to the hydrophobic microplastic particles and to leave aside the hydrophilic silica surface. Additional proof-of-concept experiments in the SI (Figure S17c-d) show the separation of PMMA particles by MNP from fine quartz particles in tap water. The water purification is visualized in Figure S17a, b. Due to their higher relative density with respect to water, fine size range and moderate hydrophobicity, the PMMA microspheres are an example of a more challenging system for separation by flotation techniques.[59] That means, if the carrier flotation tests are successful for

this model system, this method will be promising for other types of plastic material such as polystyrene (Figure S18).

5. CONCLUSIONS

We used oleate stabilized magnetic nanoparticles for model experiments on carrier flotation of microplastic (PMMA) particles. We showed that the MNP can be magnetically aggregated and demonstrate magnetophoresis-induced convection in external magnetic fields. The magnetic aggregation of the MNP is dependent on the ionic strength of the suspension. Heteroagglomeration of MNP and PMMA was achieved by their relative velocity in a flow field causing collision and attachment of MNP on the PMMA surface. The formed MNP-PMMA complexes could be further aggregated and collected with the help of permanent magnets. Our results on the influence of the stirring speed on the size of the formed aggregates may contribute to the hydrodynamic optimization of future separation reactors.

In the field of water purification, magnetic iron oxide nanoparticles up to now were mainly used as adsorbents due to their high specific surface area, e.g. for heavy metal

ions.[60] First approaches to remove microplastic material by magnetic micro- or nanoparticles only were described very recently. The employed magnetic particle systems focused on rather specific functionality[61,62] or on the applicability to a broad spectrum of environmental sample materials including common microplastic types like polystyrene or polyethylene.[63,64] We deepen the important findings from literature,[61–64] by a defined variation of electrolyte background, insights into the dynamic microprocesses for a simple MNP material, and interactions with the hydrodynamic conditions not considered in the previous studies.

Our observations suggest that the MNP aggregate structure has significant influence on the separation process. It is known that the aggregate structure is affected by the shape of the MNP,[65] the composition and hydrodynamics in the surrounding aqueous phase.[66] In turn, the agglomerate structure influences the selectivity of the separation process. Highly branched shapes might lead to a facilitated network formation, but to a reduced selectivity towards the target material due to the higher probability of inclusions of unwanted substances. An appealing aspect for future work is to optimize this tradeoff through the aggregation kinetics. The composition of the aqueous phase changes the

particle surface properties, the particle-particle interactions and hence the aggregation kinetics. From the hydrodynamic point of view, the interplay of particle attachment and detachment affects the developing aggregate form and possible inclusions. Along with the structure of the magnetic field, several control parameters are available to shape the aggregates for better performance of the overall process.

ASSOCIATED CONTENT

Supporting Information.

The following files are available free of charge.

Calculations of colloidal stability (van der Waals forces and electrostatic forces) of nanoparticles at different ionic strengths. Calculations of aggregation parameter and magnetic Grashof number. Illustration of setups for measuring the sedimentation velocities and the particle size distributions during heteroagglomeration of MNP and PMMA spheres. Calculation of magnetic flux density along the optical beam axis within the cuvette used for laser diffraction particle size measurements. Hydrodynamic

diameter distributions and median diameter of oleate coated nanoparticles at different salt concentrations derived from DLS. Sedimentation velocities with and without magnetic fields at different salt concentrations. Calculated interaction energies and coupling parameters. Temporal evolutions of particle size distributions during mixing for PMMA and PMMA + MNP suspensions. Illustration of water purification by magnetic carrier flotation. Heteroagglomeration of polystyrene spheres with MNP. (file type, PDF)

V1_Sedimentation.avi: Increasing surface coverage during settling of PMMA microspheres through diluted MNP dispersion. The width of the field of view is 0.48 mm. The video playback speed is in real-time. (file type, AVI)

V2_Reversal.avi: Sedimentation movement of MNP-PMMA clusters is reversed by applying a small magnet (NdFeB N 42 magnet with diameter 4 mm, height 6 mm) above the field of view, and magnet-induced aggregation occurs. After the magnet is removed at the end of the video, the formed larger agglomerates disaggregate and sedimentation resumes. The width of the field of view is 0.48 mm. The video playback speed is in real-time.

V3_Magnet_dia1.avi: Bulky MNP-PMMA clusters appearing when a larger magnet (NdFeB N 42 magnet with diameter 10 mm, height 10 mm) is applied above the field of view. The width of the field of view is 0.48 mm. The video playback speed is in real-time.

AUTHOR INFORMATION

Corresponding Author

*E-mail: s.schwaminger@tum.de

*E-mail: k.schwarzenberger@hzdr.de

*E-mail: k.eckert@hzdr.de

Present Addresses

†Department of Chemical Engineering, Massachusetts Institute of Technology, 77 Massachusetts Avenue, Cambridge, MA 02139, USA

Author Contributions

The manuscript was written through contributions of all authors. All authors have given approval to the final version of the manuscript. #These authors contributed equally.

ACKNOWLEDGMENT

We would like to thank Prof. Sonja Berensmeier for laboratory resources and valuable discussions. We acknowledge Dr. Carsten Peters for help with transmission electron microscopy. Furthermore, we thank Prof. Tom Nilges and Prof. Thomas Fässler for provision of XRD and SQUID, respectively. Thomas Nothhaft is acknowledged for his support on the laboratory work. Leonie Wittmann is acknowledged for her support on the visualisation. The Dr.-Ing. Leonhard-Lorenz foundation is acknowledged for financial support of equipment and material costs. Financial support was provided by the German Helmholtz Association and the German Aerospace Center (DLR) with funds provided by the Federal Ministry for Economic Affairs and Energy (BMWi) due to an enactment of the German Bundestag under Grant No. DLR 50WM2059 (Project MAGSOLEX).

ABBREVIATIONS

ATR FTIR, attenuated total reflection Fourier transformation infrared; DLS, dynamic light scattering; DLVO, Derjaguin, Landau, Verwey, Overbeek; FWHM, full width at half maximum; JCPDS, Joint Committee on Powder Diffraction Standards; MNP, magnetic nanoparticles; OC, optical centrifuge; PMMA, poly(methyl methacrylate); SQUID superconducting quantum interference device; TEM, transmission electron microscopy; XRD, X-Ray diffraction

REFERENCES

(1) Laurent, S.; Forge, D.; Port, M.; Roch, A.; Robic, C.; Vander Elst, L.; Muller, R. N. Magnetic Iron Oxide Nanoparticles: Synthesis, Stabilization, Vectorization, Physicochemical Characterizations, and Biological Applications. *Chem. Rev.* **2008**, *108*, 2064–2110.

(2) Park, J.; An, K.; Hwang, Y.; Park, J.-G.; Noh, H.-J.; Kim, J.-Y.; Park, J.-H.; Hwang, N.-M.; Hyeon, T. Ultra-Large-Scale Syntheses of Monodisperse Nanocrystals. *Nat. Mater.* **2004**, *3*, 891–895.

(3) Lu, A.-H.; Salabas, E. L.; Schüth, F. Magnetic Nanoparticles: Synthesis, Protection, Functionalization, and Application. *Angew. Chem. Int. Ed.* **2007**, *46*, 1222–1244.

(4) Roth, H.-C.; Schwaminger, S. P.; Schindler, M.; Wagner, F. E.; Berensmeier, S. Influencing Factors in the Co-Precipitation Process of Superparamagnetic Iron Oxide Nano Particles: A Model Based Study. *J. Magn. Magn. Mater.* **2015**, *377*, 81–89.

(5) Schwaminger, S. P.; Syhr, C.; Berensmeier, S. Controlled Synthesis of Magnetic Iron Oxide Nanoparticles: Magnetite or Maghemite? *Crystals* **2020**, *10*, 214.

(6) Bronstein, L. M.; Huang, X.; Retrum, J.; Schmucker, A.; Pink, M.; Stein, B. D.; Dragnea, B. Influence of Iron Oleate Complex Structure on Iron Oxide Nanoparticle Formation. *Chem. Mater.* **2007**, *19*, 3624–3632.

(7) Chen, M. J.; Shen, H.; Li, X.; Liu, H. F. Facile Synthesis of Oil-Soluble Fe3O4 Nanoparticles based on a Phase Transfer Mechanism. *Appl. Surf. Sci.* **2014**, *307*, 306–310.

(8) Bloemen, M.; Brullot, W.; Luong, T. T.; Geukens, N.; Gils, A.; Verbiest, T. Improved Functionalization of Oleic Acid-Coated Iron Oxide Nanoparticles for Biomedical Applications. *J. Nanopart. Res.* **2012**, *14*, 1100.

(9) Zhu, R.; Liu, M.; Hou, Y.; Zhang, L.; Li, M.; Wang, D.; Fu, S. One-Pot Preparation of Fluorine-Free Magnetic Superhydrophobic Particles for Controllable Liquid Marbles and Robust Multifunctional Coatings. *ACS Appl. Mater. Interfaces* **2020**, *12*, 17004–17017.

(10) Padwal, P.; Finger, C.; Fraga-García, P.; Kaveh-Baghbaderani, Y.; Schwaminger, S. P.; Berensmeier, S. Seeking Innovative Affinity Approaches: A Performance Comparison between Magnetic Nanoparticle Agglomerates and Chromatography Resins for Antibody Recovery. *ACS Appl. Mater. Interfaces* **2020**, *12*, 39967–39978.

(11) Liu, J.; Dai, C.; Hu, Y. Aqueous Aggregation Behavior of Citric Acid Coated Magnetite Nanoparticles: Effects of pH, Cations, Anions, and Humic Acid. *Environ. Res.* **2018**, *161*, 49–60.

(12) Ezzaier, H.; Marins, J. A.; Claudet, C.; Hemery, G.; Sandre, O.; Kuzhir, P. Kinetics of Aggregation and Magnetic Separation of Multicore Iron Oxide Nanoparticles: Effect of the Grafted Layer Thickness. *Nanomaterials* **2018**, *8*.

(13) Roth, H.-C.; Schwaminger, S.; Fraga García, P.; Ritscher, J.; Berensmeier, S. Oleate Coating of Iron Oxide Nanoparticles in Aqueous Systems: the Role of Temperature and Surfactant Concentration. *J. Nanopart. Res.* **2016**, *18*, 303.

(14) Shen, L.; Laibinis, P. E.; Hatton, T. A. Bilayer Surfactant Stabilized Magnetic Fluids: Synthesis and Interactions at Interfaces. *Langmuir* **1999**, *15*, 447–453.

(15) Schwaminger, S. P.; Fraga-García, P.; Eigenfeld, M.; Becker, T. M.; Berensmeier, S. Magnetic Separation in Bioprocessing Beyond the Analytical Scale: From Biotechnology to the Food Industry. *Front. Bioeng. Biotechnol.* **2019**, *7*, 233.

(16) Panja, S.; Maji, S.; Maiti, T. K.; Chattopadhyay, S. A Smart Magnetically Active Nanovehicle for on-Demand Targeted Drug Delivery: Where van der Waals Force Balances the Magnetic Interaction. *ACS Appl. Mater. Interfaces* **2015**, *7*, 24229–24241.

(17) Palma, R. de; Peeters, S.; van Bael, M. J.; van den Rul, H.; Bonroy, K.; Laureyn, W.; Mullens, J.; Borghs, G.; Maes, G. Silane Ligand Exchange to Make Hydrophobic Superparamagnetic Nanoparticles Water-Dispersible. *Chem. Mater.* **2007**, *19*, 1821–1831.

(18) Paria, S.; Khilar, K. C. A Review on Experimental Studies of Surfactant Adsorption at the Hydrophilic Solid-Water Interface. *Adv. Colloid Interface Sci.* **2004**, *110*, 75–95.

(19) Wooding, A.; Kilner, M.; Lambrick, D. B. Studies of the Double Surfactant Layer Stabilization of Water-Based Magnetic Fluids. *J. Colloid Interface Sci.* **1991**, *144*, 236–242.

(20) Leong, S. S.; Ahmad, Z.; Lim, J. Magnetophoresis of Superparamagnetic Nanoparticles at Low Field Gradient: Hydrodynamic Effect. *Soft Matter* **2015**, *11*, 6968–6980.

(21) Leong, S. S.; Ahmad, Z.; Low, S. C.; Camacho, J.; Faraudo, J.; Lim, J. Unified View of Magnetic Nanoparticle Separation under Magnetophoresis. *Langmuir* **2020**, *36*, 8033–8055.

(22) Orlandi, G.; Kuzhir, P.; Izmaylov, Y.; Alves Marins, J.; Ezzaier, H.; Robert, L.; Doutre, F.; Noblin, X.; Lomenech, C.; Bossis, G.; Meunier, A.; Sandoz, G.; Zubarev, A. Microfluidic Separation of Magnetic Nanoparticles on an Ordered Array of Magnetized Micropillars. *Phys. Rev. E* **2016**, *93*, 62604.

(23) McNab, B.; Jankovic, A.; David, D.; Payne, P. Processing of Magnetite Iron Ores – Comparing Grinding Options. *Iron Ore Conf.* **2009**.

(24) Lu, L. *Iron Ore*; Woodhead Publishing, 2015.

(25) Araujo, A. C.; Amarante, S. C.; Souza, C. C.; Silva, R. R. R. Ore Mineralogy and Its Relevance for Selection of Concentration Methods in Processing of Brazilian Iron Ores. *Miner. Process. Extr. Metall.* **2003**, *112*, 54–64.

(26) Kulkarni, R. D.; Somasundaran, P. Flotation Chemistry of Hematite/Oleate System. *Colloids Surf.* **1980**, *1*, 387–405.

(27) Mathur, S. Kaolin Flotation. *J. Colloid Interface Sci.* **2002**, *256*, 153–158.

(28) Eckert, K.; Schach, E.; Gerbeth, G.; Rudolph, M. Carrier Flotation: State of the Art and its Potential for the Separation of Fine and Ultrafine Mineral Particles. *Mater. Sci. Forum* **2019**, *959*, 125–133.

(29) Anastassakis, G. N. A Study on the Separation of Magnesite Fines by Magnetic Carrier Methods. *Colloids Surf. A* **1999**, *149*, 585–593.

(30) Anastassakis, G. N. Separation of Fine Mineral Particles by Selective Magnetic Coating. *J. Colloid Interface Sci.* **2002**, *256*, 114–120.

(31) Broomberg, J.; Gélinas, S.; Finch, J. A.; Xu, Z. Review of Magnetic Carrier Technologies for Metal Ion Removal. *Magn. Electr. Sep.* **1999**, *9*, 169–188.

(32) Parsonage, P. Principles of Mineral Separation by Selective Magnetic Coating. *Int. J. Miner. Process.* **1988**, *24*, 269–293.

(33) Diez, M.; Gökpekin, A.; Krieglstein, W. Method for Obtaining Non-Magnetic Ores from Suspension-Like Mass Flow Containing Non-Magnetic Ore Particles. PCT/EP2012/060218.

(34) Albijanic, B.; Ozdemir, O.; Nguyen, A. V.; Bradshaw, D. A Review of Induction and Attachment Times of Wetting Thin Films between Air Bubbles and Particles and Its Relevance in the Separation of Particles by Flotation. *Adv. Colloid Interface Sci.* **2010**, *159*, 1–21.

(35) Prochazkova, G.; Safarik, I.; Branyik, T. Harvesting Microalgae with Microwave Synthesized Magnetic Microparticles. *Biores. Technol.* **2013**, *130*, 472–477.

(36) Stange, R.; Lenk, F.; Eckert, K.; Lenk, S.; Bley, T.; Boschke, E. A New Method for Mixing of Suspended Superparamagnetic Beads Using Variable Electromagnetic Fields. *Eng. Life Sci.* **2015**, *15*, 727–732.

(37) Han, X.; Lu, X.; Vogt, R. D. An Optimized Density-Based Approach for Extracting Microplastics from Soil and Sediment Samples. *Environ. Pollut.* **2019**, *254*, 113009.

(38) Talvitie, J.; Mikola, A.; Koistinen, A.; Setälä, O. Solutions to Microplastic Pollution - Removal of Microplastics from Wastewater Effluent with Advanced Wastewater Treatment Technologies. *Water Res.* **2017**, *123*, 401–407.

(39) Falahati, H.; Wong, L.; Davarpanah, L.; Garg, A.; Schmitz, P.; Barz, D. P. J. The Zeta Potential of PMMA in Contact with Electrolytes of Various Conditions: Theoretical and Experimental Investigation. *Electrophoresis* **2014**, *35*, 870–882.

(40) Köhler, U.; Stübinger, T.; Witt, W. Laser-Diffraction Results from Dynamic Image Analysis Data. *WCPT62010*.

(41) Schwaminger, S. P.; Bauer, D.; Fraga-García, P.; Wagner, F. E.; Berensmeier, S. Oxidation of Magnetite Nanoparticles: Impact on Surface and Crystal Properties. *CrystEngComm* **2017**, *19*, 246–255.

(42) Schwaminger, S. P.; Fraga-García, P.; Selbach, F.; Hein, F. G.; Fuß, E. C.; Surya, R.; Roth, H.-C.; Blank-Shim, S. A.; Wagner, F. E.; Heissler, S.; Berensmeier, S. Bio-Nano Interactions: Cellulase on Iron Oxide Nanoparticle Surfaces. *Adsorption* **2017**, *23*, 281–292.

(43) Wang, X.; Zhang, C.; Wang, X.; Gu, H. The Study on Magnetite Particles Coated with Bilayer Surfactants. *Appl. Surf. Sci.* **2007**, *253*, 7516–7521.

(44) Schwaminger, S. P.; Blank-Shim, S. A.; Scheifele, I.; Pipich, V.; Fraga-García, P.; Berensmeier, S. Design of Interactions Between Nanomaterials and Proteins: A Highly

Affine Peptide Tag to Bare Iron Oxide Nanoparticles for Magnetic Protein Separation. *Biotechnol. J.* **2019**, *14*, e1800055.

(45) Roonasi, P.; Holmgren, A. A Fourier Transform Infrared (FTIR) and Thermogravimetric Analysis (TGA) Study of Oleate Adsorbed on Magnetite Nano-Particle Surface. *Appl. Surf. Sci.* **2009**, *255*, 5891–5895.

(46) Yang, K.; Peng, H.; Wen, Y.; Li, N. Re-Examination of Characteristic FTIR Spectrum of Secondary Layer in Bilayer Oleic Acid-Coated Fe3O4 Nanoparticles. *Appl. Surf. Sci.* **2010**, *256*, 3093–3097.

(47) Jiang, W.; Wu, Y.; He, B.; Zeng, X.; Lai, K.; Gu, Z. Effect of Sodium Oleate as a Buffer on the Synthesis of Superparamagnetic Magnetite Colloids. *J. Colloid Interface Sci.* **2010**, *347*, 1–7.

(48) Rudolph, M.; Erler, J.; Peuker, U. A. A TGA–FTIR Perspective of Fatty Acid Adsorbed on Magnetite nanoparticles–Decomposition steps and magnetite reduction. *Colloids Surf. A* **2012**, *397*, 16–23.

(49) Ramimoghadam, D.; Bagheri, S.; Hamid, S. B. A. In-situ Precipitation of Ultra-Stable Nano-Magnetite Slurry. *J. Magn. Magn. Mater.* **2015**, *379*, 74–79.

(50) Jovanović, S.; Spreitzer, M.; Tramšek, M.; Trontelj, Z.; Suvorov, D. Effect of Oleic Acid Concentration on the Physicochemical Properties of Cobalt Ferrite Nanoparticles. *J. Phys. Chem. C* **2014**, *118*, 13844–13856.

(51) Roonasi, P.; Yang, X.; Holmgren, A. Competition between Sodium Oleate and Sodium Silicate for a Silicate/Oleate Modified Magnetite Surface Studied by in situ ATR-FTIR Spectroscopy. *J. Colloid Interface Sci.* **2010**, *343*, 546–552.

(52) Babick, F.; Schießl, K.; Stintz, M. Characterization of Pyrogenic Powders with Conventional Particle Sizing Technique: I. Prediction of Measured Size Distributions. *Part. Part. Syst. Charact.* **2012**, *29*, 104–115.

(53) Ng, W. M.; Katiyar, A.; Mathivanan, V.; Teng, X. J.; Leong, S.; Low, S.; Lim, J. Sedimentation Kinetics of Magnetic Nanoparticle Clusters: Iron Oxide Nanospheres vs Nanorods. *Langmuir* **2020**, *36*, 5085–5095.

(54) Mykhaylyk, O.; Lerche, D.; Vlaskou, D.; Schoemig, V.; Detloff, T.; Krause, D.; Wolff, M.; Joas, T.; Berensmeier, S.; Plank, C. Magnetophoretic Velocity Determined by Space- and Time-Resolved Extinction Profiles. *IEEE Magn. Lett.* **2015**, *6*, 1–4.

(55) Vicente, J. de; Klingenberg, D. J.; Hidalgo-Alvarez, R. Magnetorheological Fluids: a Review. *Soft Matter* **2011**, *7*, 3701.

(56) Khademi, M.; Wang, W.; Reitinger, W.; Barz, D. P. J. Zeta Potential of Poly(methyl methacrylate) (PMMA) in Contact with Aqueous Electrolyte-Surfactant Solutions. *Langmuir* **2017**, *33*, 10473–10482.

(57) Dong, X.; Price, M.; Dai, Z.; Xu, M.; Pelton, R. Mineral-Mineral Particle Collisions during Flotation Remove Adsorbed Nanoparticle Flotation Collectors. *J. Colloid Interface Sci.* **2017**, *504*, 178–185.

(58) Liu, Q.; Friedlaender, F. J. Fine Particle Processing by Magnetic Carrier Methods. *Miner. Eng.* **1994**, *7*, 449–463.

(59) Wang, J.; Wang, H.; Wang, C.; Zhang, L.; Wang, T.; Zheng, L. A Novel Process for Separation of Hazardous Poly(Vinyl Chloride) from Mixed Plastic Wastes by Froth Flotation. *Waste Manage.* **2017**, *69*, 59–65.

(60) Yeap, S. P.; Lim, J.; Ooi, B. S.; Ahmad, A. L. Agglomeration, Colloidal Stability, and Magnetic Separation of Magnetic Nanoparticles: Collective Influences on Environmental Engineering Applications. *J. Nanopart. Res.* **2017**, *19*, 2336.

(61) Sun, M.; Chen, W.; Fan, X.; Tian, C.; Sun, L.; Xie, H. Cooperative Recyclable Magnetic Microsubmarines for Oil and Microplastics Removal from Water. *Appl. Mater. Today* **2020**, *20*, 100682.

(62) Wang, L.; Kaeppler, A.; Fischer, D.; Simmchen, J. Photocatalytic TiO2 Micromotors for Removal of Microplastics and Suspended Matter. *ACS Appl. Mater. Interfaces* **2019**, *11*, 32937–32944.

(63) Grbic, J.; Nguyen, B.; Guo, E.; You, J. B.; Sinton, D.; Rochman, C. M. Magnetic Extraction of Microplastics from Environmental Samples. *Environ. Sci. Technol. Lett.* **2019**, *6*, 68–72.

(64) Misra, A.; Zambrzycki, C.; Kloker, G.; Kotyrba, A.; Anjass, M. H.; Franco Castillo, I.; Mitchell, S. G.; Güttel, R.; Streb, C. Water Purification and Microplastics Removal Using Magnetic Polyoxometalate-Supported Ionic Liquid Phases (magPOM-SILPs). *Angew. Chem. Int. Ed.* **2020**, *59*, 1601–1605.

(65) Lim, J. K.; Chieh, D. C. J.; Jalak, S. A.; Toh, P. Y.; Yasin, N. H. M.; Ng, B. W.; Ahmad, A. L. Rapid Magnetophoretic Separation of Microalgae. *Small* **2012**, *8*, 1683–1692.

(66) Luo, L.; Nguyen, A. V. A Review of Principles and Applications of Magnetic Flocculation to Separate Ultrafine Magnetic Particles. *Sep. Purif. Technol.* **2017**, *172*, 85–99.

For Table of Contents Only

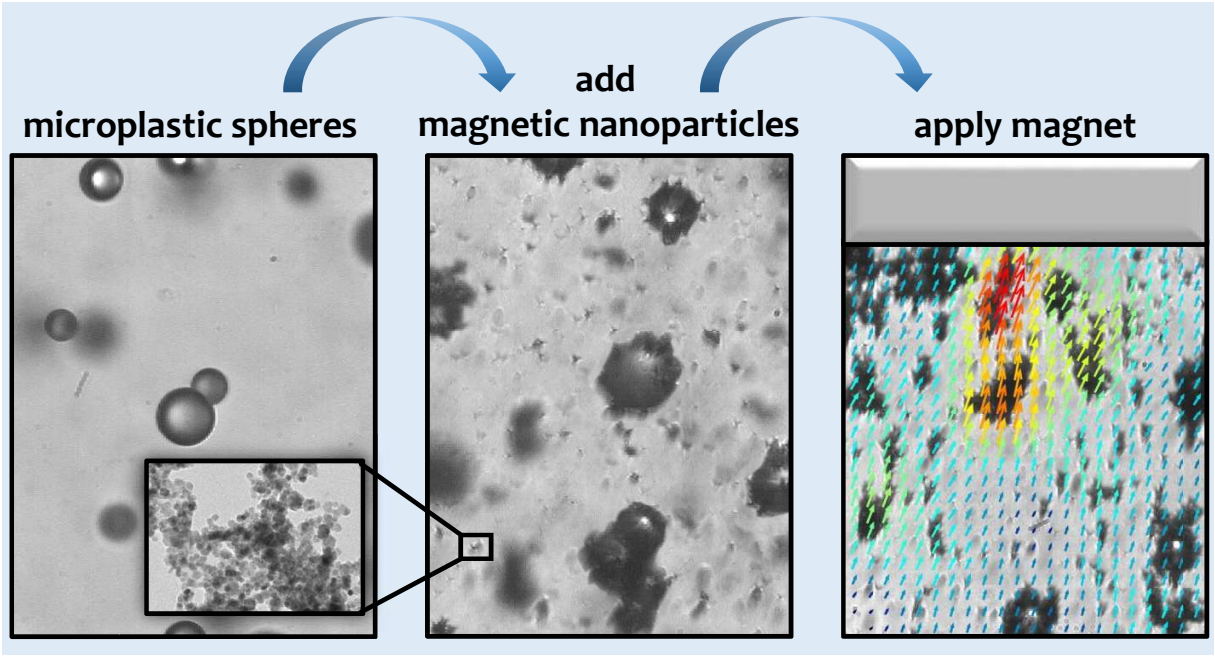
add
microplastic spheres
magnetic nanoparticles
apply magnet